Boundary-Layer Meteorol
DOI 10.1007/s10546-016-0130-4

ORIGINAL ARTICLE

Sampling the Structure of Convective Turbulence and Implications for Grey-Zone Parametrizations

Rachel Honnert[1] · **Fleur Couvreux**[1] · **Valéry Masson**[1] · **Dávid Lancz**[2]

Received: 22 May 2015 / Accepted: 12 January 2016

Abstract The grey zone of dry convection is the range of scales in which boundary-layer thermals are partly explicitly resolved by numerical weather prediction (NWP) models and partly parametrized. We seek to determine how thermals are divided into subgrid and resolved scales in the grey zone of convective boundary-layer thermals. Reference data for grid-scale and subgrid-scale fields at these resolutions are constructed by filtering 62.5-m large-eddy simulation data. A conditional sampling is adapted to detect subgrid thermals, and is used to characterize the subgrid thermals at several grid spacings in the grey zone. A mass-flux parametrization used in NWP models is compared with the subgrid thermal field. The analysis demonstrates that, although the mass-flux framework is suitable in the grey zone, some assumptions of the mass-flux schemes, usually used at the mesoscale, cannot be made in the grey zone. In particular, the thermal fraction is not small, the resolved vertical velocity is not negligible, the entrainment and detrainment rates depend on the horizontal resolution, the triggering and the closure at the surface are moreover random.

Keywords Convective boundary layer · Grey zone · Large-eddy simulation · Mass-flux scheme

1 Introduction

In the atmosphere, wind shear and buoyancy forces generate random eddy motions. Atmospheric boundary-layer turbulent eddies range from the kilometric to the millimetric scale and are currently well-represented by two types of model that differ from each other in their horizontal grid size. On the one hand, in large-eddy simulations (LES) (Deardorff 1972) in which the grid spacing is on the order of 10 m, the turbulence is mainly resolved,while the

✉ Rachel Honnert
rachel.honnert@meteo.fr

1 CNRM, Météo-France, 42, Avenue Gaspard Coriolis, 31057 Toulouse Cedex 01, France

2 Hungarian Meteorological Service, Kitaibel Pál u.1., Budapest 1024, Hungary

Published online: 24 February 2016

residual turbulence is generally assumed homogeneous and isotropic. This is parametrized using the eddy diffusivity, which represents local mixing by small-scale turbulence. On the other hand, in current numerical weather prediction (NWP) models, the turbulence is entirely subgrid, thus entirely parametrized.

At these scales, the eddy diffusivity representation cannot represent the convective boundary-layer (CBL) counter-gradient zone (Deardorff 1972). This zone is rather parametrized by methods such as the use of the counter-gradient (Deardorff 1972), the transilient matrix (Stull 1984) or the mass-flux scheme (Hourdin et al. 2002; Siebesma et al. 2007). Frech and Mahrt (1995) proposed splitting the fluxes into local and non-local parts and to parametrize them separately. Although these so-called two-scale mixing formulations are physically oversimplified, they are now often used in particular in the eddy-diffusivity/mass-flux (EDMF) concept that consists of combining a mass-flux scheme representing the effect of coherent structures with a parametrization for the small-scale turbulence based on eddy diffusivity. For instance, in the Méso-NH model (Lafore et al. 1998), the EDMF concept relies on the turbulence scheme of Cuxart et al. (2000) where the local turbulence is represented by an eddy diffusivity and the non-local turbulence is represented by the mass-flux scheme of Pergaud et al. (2009) (hereafter PM09).

Increasingly, numerical mesoscale models are now operating at horizontal resolutions in the range 500 m to 2 km, and in CBL cases, they therefore reach the range of resolution termed "Terra Incognita" (Wyngaard 2004) also referred to as the "grey zone" of boundary-layer thermals, for which the horizontal grid spacing is on the order of the size of the largest boundary-layer turbulent structures (the convective thermals). At these scales, the largest CBL structures are neither entirely resolved nor entirely subgrid.

By filtering LES, Honnert et al. (2011) constructed reference data providing the subgrid/resolved partitioning of fluxes and variances in convective cases. In fact, they showed that this partitioning depends on $\Delta x/(h + h_c)$, where Δx is the horizontal grid spacing, h is the boundary-layer height (defined as the height of the minimum of the buoyancy flux) and h_c is the height of the cloud layer (defined as the layer where the mean liquid water is larger than 10^{-5}g kg^{-1}). These results have been confirmed and extended to cases with increasing wind shear by Shin and Hong (2013). Using the reference partitioning, Honnert et al. (2011) tested the various turbulence parametrizations of the Méso-NH model : varying the mixing length of the turbulent kinetic energy (TKE) scheme, taking into account or not the horizontal gradient (1D or 3D turbulence scheme (see Cuxart et al. (2000) for more details) and activating or not a mass-flux scheme (Pergaud et al. 2009).

They showed that, whatever the configuration of the turbulence scheme, the grey zone ($0.2 \leq \Delta x(h + h_c) \leq 2$) is poorly represented, and the impact of the configuration is undeniable. The activation of the mass-flux scheme has the most significant impact, and when it is deactivated, the subgrid mixing is too weak, resulting in resolved structures that are too large and too strong. In contrast, when the scheme is activated, the resolved variability disappears, as the mass flux simulates the behaviour of several entirely subgrid structures whereas it should simulate at least one partly resolved thermal. So, the representation of the thermals appears to be the main problem in the grey zone, as thermals are partly resolved and partly subgrid. Ideally, these parametrizations should be consistent with the large-scale parametrization on the one hand, and with the LES parametrization on the other.

Using a mass-flux parametrization in the grey zone of CBL thermals remains attractive as the size decomposition allows the mass-flux contribution of the thermals to be modified, while the local eddy-diffusivity component remains unchanged. Note that the local eddy diffusivity is also often used as a parametrization for the small-scale turbulence in LES, which suggests that it should remain unchanged. Some assumptions of the mass-flux scheme in the grey

zone of deep convection, i.e. the mesoscale (2–10 km), have been revisited by Arakawa et al. (2011). They explained that the assumption of a small fractional area covered by convective clouds in mass-flux parametrizations may not be verified in the grey zone of convection and must be suppressed. They also showed that the mass-flux framework is adapted to the grey zone of convection. A similar criticism and adaptation of the mass-flux scheme must be done in the grey zone of CBL thermals. However, this requires determination of which part of the thermal flux must be produced by the turbulence scheme, and therefore a definition of what is a subgrid thermal in the grey zone of CBL thermals, which is the focus of this study.

Shin and Hong (2013) used conditional sampling in order to separate thermals in a LES from their environment, and thus the local and non-local turbulent transport. Although their work provides results on the non-local flux, it does not provide any information on the structure of the thermal. Especially the exchanges of in-thermal air with the environment are critical features for mass-flux parametrizations. The objective is thus to adapt a conditional sampling to the grey zone in order to provide information on the subgrid thermals in the grey zone and recommendations for future parametrizations.

The article is organized as follows: in Sect. 2, a conditional sampling is adapted to define the subgrid thermal in the grey zone of CBL thermals. In Sect. 3, this new tool is used to quantify the thermal characteristics, while Sect. 4 examines the validity of the mass-flux scheme equations in the grey zone. Finally, Sect. 5 presents a summary.

2 Method and Tools

As shown by Honnert et al. (2011), in the grey zone, the default of mass-flux parametrization schemes is to simulate entirely subgrid thermals even when very fine grids are used, while part of the thermal effects should be resolved. To adapt mass-flux schemes at these resolutions, we have to know the characteristics of the non-local turbulence that is still subgrid in the grey zone. The question arises as to what defines a subgrid thermal in the grey zone of CBL thermals. And first of all, how can subgrid thermals be detected? LES of the convective boundary layer provides mainly resolved thermals, and these simulated thermals can be isolated from their environment using conditional sampling. In our study, a conditional sampling is adapted to detect the subgrid component of the thermals at a given grid spacing. Notations are defined in Appendix 1.

2.1 Reference Data: LES

2.1.1 Model Description

The Méso-NH model (Lafore et al. 1998) is used to simulate CBL cases, with simulations performed on a $16 \times 16 \times 5\,\mathrm{km}^3$ domain. According to De Roode et al. (2004), the dominant length scale in a clear CBL without moisture is on the order of (or twice) the boundary-layer height; if clouds are included, the dominant length scale increases. Here, LES are performed on a $16 \times 16\ \mathrm{km}^2$ horizontal domain size, which is large enough to resolve large-scale fluctuations, since the boundary-layer height is always <2.5 km. The horizontal grid size is 62.5 m. Vertical grid sizes vary depending on the simulated case, but the vertical grid spacing is always <100 m in the CBL, so that the grid boxes are close to cubic. Initial profiles for potential temperature, water vapour mixing ratio and wind speed, as well as prescribed surface fluxes, are derived from observations for the five experimental cases detailed in Sect. 2.1.2. A

Table 1 Modelled CBL mean values over the duration of the simulations of: analysed duration, averaged CBL height, averaged cloud-base height (ZCB), averaged surface buoyancy flux (H_{0v}), averaged surface humidity flux (E_0), convective velocity scale (w_*), friction velocity (u_*), Obukhov length (L_O) and ratio of the averaged CBL height over the Obukhov length

	Duration (h)	h (m)	ZCB (m)	H_{0v} (m s^{-1}K)	E_0 (m s^{-1})	w_* (m s^{-1})	u_* (m s^{-1})	L_O (m)	$\frac{-h}{L_O}$
IHOP$_{2002}$	5	1046		0.17	6×10^{-5}	1.78	0.29	−12	94
Wangara	4	1203		0.17	2×10^{-5}	1.9	0.05	−0.11	4715
AMMA	4	1819		0.34	0	2.66	0.34	−10	225
BOMEX	8	580	540	0.08	5×10^{-5}	0.52	0.28	−220	2.4
ARM	7	1076	1020	0.09	1×10^{-5}	1.37	0.46	−8.3	10.9

tri-dimensional turbulence scheme using the Deardorff length scale (grid size, limited by the stability (Cuxart et al. 2000) simulates the small three-dimensional eddies. The LES results are used as a reference hereafter.

2.1.2 Benchmark Simulations

We use three dry CBL cases and two cases of the cumulus non-drizzling CBL. As attested by the spread in boundary-layer height, surface fluxes, friction velocities, and Obukhov length, presented in Table 1, these cases represent a large range of conditions. The first case (IHOP) is derived from the International H_2O project (Weckwerth et al. 2004), and corresponds to a clear continental growing CBL reaching 1.5 km in height with low winds and weak vertical shear (see Couvreux et al. 2005 for details). The second case (Wangara) is derived from the Wangara campaign (Clarke et al. 1971), conducted in July and August 1967 at Hay, Australia. The last dry case (AMMA) is derived from the African Monsoon Multidisciplinary Analysis field campaign (Redelsperger et al. 2006); it has a heat flux twice as large as in the previous simulations (Canut et al. 2012). These cases have been extensively validated against observations (see Couvreux et al. 2005; Canut et al. 2012). The first two hours of all simulations are considered spin-up. Since the wind is strong at the beginning of the AMMA simulation, the following 2 h are also removed from this case, as we wish to focus solely on free convective conditions ($-h/L_O \geq 50$, with L_O the Obukhov length as defined by Deardorff 1972).

In addition, two cases of a cumulus-topped non-drizzling CBL are simulated. The first case is derived from the Barbados Oceanographic and Meteorologic EXperiment (BOMEX) and corresponds to oceanic shallow cumulus (Siebesma et al. 2003). The second is based on an idealization of the experiment situated at the Southern Great Plains site of the Atmospheric Radiation Measurement (ARM) Program ; Brown et al. (2002) presents this case of cloudy convection over land.

2.1.3 Averaging Procedure

The horizontal grid spacing of the LES, 62.5 m, ensures that the main turbulence structures are resolved. To check that the turbulence was mainly resolved, simulations have been performed at heights of 62.5, 125, 250, and 500 m (not shown) and we have checked that the total TKE

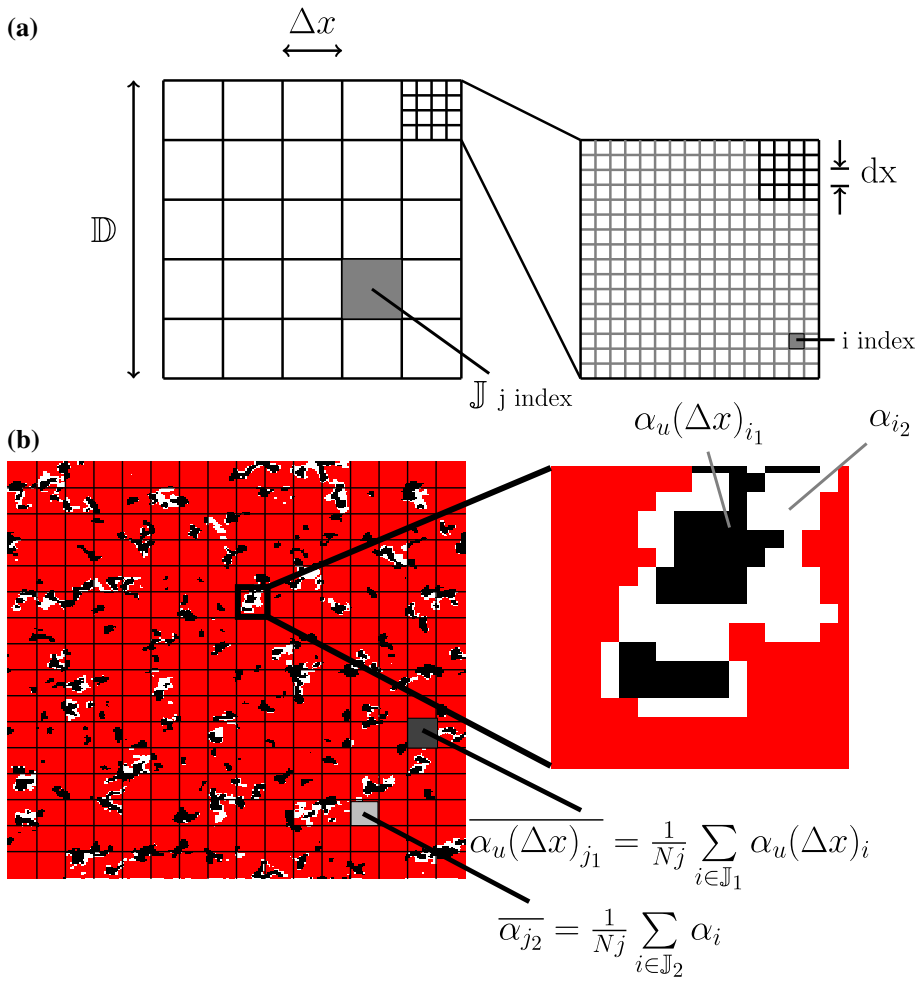

Fig. 1 **a** Schematic diagram presenting the different scales considered: $\mathbb{D}$ is the whole domain; Δx is the grid length at which the diagnostics are calculated; $\mathbb{J}$ is a domain of Δx size; dx is the LES grid size; i and j are respectively the indices of the LES grid and the Δx resolution grid; N is the number LES cells in $\mathbb{D}$ and N_j is the number LES cells in a $\mathbb{J}$ domain. **b** LES (IHOP case , 1400 LT, 500-m altitude) horizontal cross-section and zoom of the thermal fraction α_i (in *white*), the subgrid thermal fraction $\alpha_u(\Delta x)_i$ (in *black*) and the environment (in *red*). See text for more details

reaches an asymptote when the grid mesh becomes smaller than 150 m in agreement with Sullivan and Patton (2008), suggesting that a LES 62.5-m grid size is a good reference. This is also in agreement with Cheng et al. (2009), who looked at the sensitivity to horizontal grid spacing from 50 to 4000 m (Honnert et al. 2011). Results have been double checked by comparing them to a LES at 31.25 m of the IHOP case (not shown). The fact that such different simulations provided similar results is also a proof of the consistency of the data (see Fig. 2). The resolved fields at a coarser resolution (Δx) are derived from the LES fields, by averaging these fields over a $\Delta x \times \Delta x$ horizontal domain at each vertical level (cf. Fig. 1a). The thermals are mainly vertically coherent structures. Therefore, the 2D fields present a lot of similarities from one level to the other ensuring that horizontal averaging is apprioriate

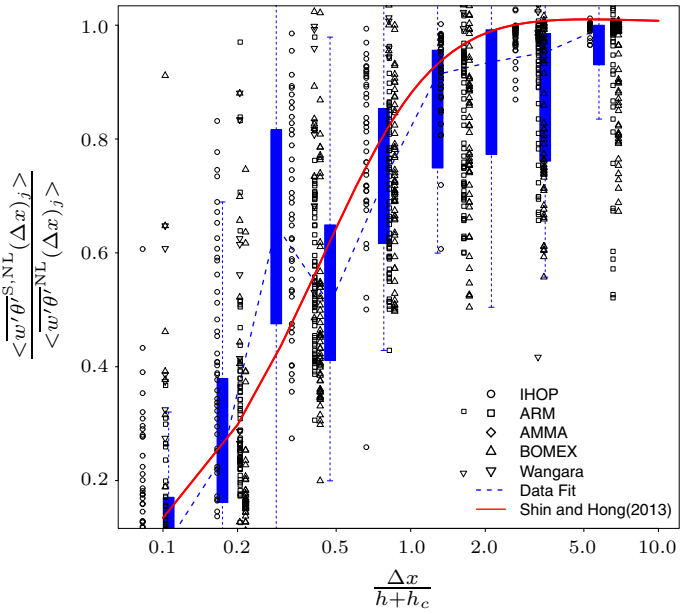

Fig. 2 Ratio of the subgrid non-local flux and the total non-local flux of potential temperature calculated for the CS_{gz} approach of the whole domain as a function of the normalized horizontal resolution for the five LES cases : IHOP at 1400 LT, AMMA at 1200 LT, ARM at 1000 LT, Wangara at 1400 LT and BOMEX at 1000 LT. Only altitudes between $z = 0.2h$ and $z = 0.8h$ are shown. Boxplots are indicated in *blue* with the mean in *dashed line*. The curve fit of Shin and Hong (2013) (cf. Eq. 11) is shown in *red*

for our study. It provides resolved fields over grid spacings from 125 m to 8 km ; see also Honnert et al. (2011) for more details.

2.2 Thermal Plume Detection

At the mesoscale, the thermal fraction is small (see large horizontal cross-section in Fig. 1b). At resolutions in the grey zone of CBL thermals, the CBL thermal fraction can be large (see large zoom in Fig. 1b) and at least a part of the updraft is resolved. In these conditions, the parametrizations must be adapted to represent the characteristics of the subgrid thermal field depending on the horizontal resolution. Here, we attempt to define these characteristics.

2.2.1 A Typical Conditional Sampling for Subgrid Thermals at the Mesoscale

Conditional samplings consider that LES grids are fine enough for their cells to be either entirely occupied by a thermal or completely void of thermals. Thus, the fractional area of the i^{th} LES cell covered by a thermal (α_i) is either 1 or 0. In order to determine which cells are "thermal" cells, the conditional sampling proposed by Couvreux et al. (2010) uses a passive tracer (whose concentration is sv) emitted at the surface, and the vertical velocity (w) to separate organized boundary-layer structures from their environment in LES of dry or cloudy boundary layers. This sampling allows characterization of the convective thermals from the surface to the top of the boundary layer in dry cases or the top of the clouds in cloudy cases. In the following, this conditional sampling is referred to as CS_{meso}, and it is defined as,

$$\alpha_i = 1 \text{ if } \begin{cases} sv_i' & > \max(\sigma_{sv}, \sigma_{min}) \\ \text{and} & w_i > 0 \end{cases}$$
$$\alpha_i = 0 \qquad \text{otherwise} \tag{1}$$

where $sv_i' = sv_i - <sv>$ is the anomaly of the concentration of the tracer, and $<sv>$ is the mean concentration of the scalar at a given vertical level,

$$<sv> = \frac{1}{N} \sum_{i \in \mathbb{D}} sv_i, \tag{2}$$

and where σ_{sv} is the standard deviation of the tracer concentration at a given vertical level calculated over the whole LES domain ($\mathbb{D}$) at each level. In particular,

$$\sigma_{sv} = \sqrt{< (sv - < sv >)^2 >} = \sqrt{\frac{1}{N} \sum_{i \in \mathbb{D}} (sv_i - < sv >)^2}, \tag{3}$$

and σ_{min} is a minimum threshold, defined as being directly proportional to the average standard deviation of the tracer concentration at lower levels. $\mathrm{CS_{meso}}$ provides a thermal fraction for the whole LES domain ($\mathbb{D}$) at each level,

$$<\alpha> = \frac{1}{N} \sum_{i \in \mathbb{D}} \alpha_i. \tag{4}$$

In the following, when $\mathrm{CS_{meso}}$ is used, the parameters or characteristics are noted as "thermal", i.e. the characteristics of the thermals in their entirety.

2.2.2 A Conditional Sampling for Subgrid Thermals in the Grey Zone

The $\mathrm{CS_{meso}}$ approach (cf. Sect. 2.2.1) separates entire thermals from their environment. However, in the grey zone of CBL thermals, only a portion of the thermals must be parametrized while the rest are resolved. Thus, the $\mathrm{CS_{meso}}$ approach does not allow a characterization of subgrid thermals in the grey zone of CBL thermals. In order to detect the part of the thermals that should be taken into account by the parametrization, this tool must be adapted to consider only the part of the thermals that is not explicitly treated by the model. When the horizontal grid spacing (Δx) of the model is in the grey zone, the subgrid part depends on Δx.

The $\mathrm{CS_{meso}}$ approach of Couvreux et al. (2010) considers that the LES cell is a thermal cell when its tracer concentration is significantly larger than the tracer concentration over the whole horizontal domain and when its vertical velocity is positive. Herein, we consider the ith LES cell to be a cell of a "subgrid thermal" when its tracer concentration is significantly larger than the resolved tracer concentration of the jth Δx resolution cell to which the ith cell belongs to (cf. Fig. 1b), and when the vertical velocity is positive and larger than the resolved vertical velocity at the Δx resolution. Consequently, the revised conditional sampling for the grey zone ($\mathrm{CS_{gz}}$) is defined as,

$$\alpha_u(\Delta x)_i = 1 \text{ if } \begin{cases} sv_i - \overline{sv}_j > max(\sigma_{sv}', \sigma_{min}') \\ \text{and } w_i > 0 \\ \text{and } w_i - \overline{w}_j > 0 \end{cases}$$
$$\alpha_u(\Delta x)_i = 0 \qquad \text{otherwise} \tag{5}$$

where $\overline{sv}_j$ and $\overline{w}_j$ are the average values of the tracer concentration and vertical velocity, respectively, over a jth cell of $\Delta x \times \Delta x$ m^2 containing the ith LES cell (cf. Fig. 1b), with

$$\overline{sv}_j = \frac{1}{N_j} \sum_{i \in \mathbb{J}} sv_i. \tag{6}$$

Now σ'_{sv} is the standard deviation of the tracer concentration at a given vertical level relative to the average value computed for the Δx cell. In particular,

$$\sigma'_{sv} = \sqrt{< (sv - \overline{sv})^2 >} = \sqrt{\frac{1}{N} \sum_{i \in \mathbb{D}} (sv_i - \frac{1}{N_j} \sum_{i \in \mathbb{J}} sv_i)^2}, \tag{7}$$

where σ'_{sv} is the average standard deviation of the tracer concentration in each Δx cell that is then averaged over the whole horizontal domain. This formulation simplifies the computation, as it is constant at one given vertical level. The direct use of the standard deviation of the tracer concentration $\sqrt{(\overline{(sv_i - \overline{sv}_j)^2})}$ provides similar conclusions for the thermal fraction and vertical velocity (cf. Sects. 3.2 and 3.3) as the average standard deviation of Eq. 7 (not shown). However the subgrid thermal field is more fragmented, less thermal-like, and does not provide the coherent entrainment/detrainment profiles shown in Sect. 3.6. σ'_{min} is the minimum threshold calculated as in CS$_{\text{meso}}$. Note that now the CS$_{\text{gz}}$ approach depends on the horizontal resolution (Δx). In the following, when the CS$_{\text{gz}}$ approach is used, the parameters or characteristics are noted as "subgrid thermal", viz. the characteristics of the subgrid thermals at one scale, as opposed to "thermal" characteristics calculated by the CS$_{\text{meso}}$ approach; $\alpha_u(\Delta x)_i$ is the subgrid thermal field at the ith LES cell, is at the LES resolution but depends on Δx.

The field $\alpha_u(\Delta x)_i$ is shown in black in Fig. 1b and included into the α field in white in Fig. 1b. In the following, the fields are calculated at the desired Δx resolution by averaging the LES fields (cf. Sect. 2.1.3) over the N_j LES cells that form a Δx cell (cf. Fig. 1a, b). The quantity $\overline{\alpha_u(\Delta x)_j}$ is the averaged value of $\alpha_u(\Delta x)_i$ over a Δx cell (cf. Fig. 1), and $\overline{\alpha_u(\Delta x)_j} \in [0, 1]$,

$$\overline{\alpha_u(\Delta x)}_j = \frac{1}{N_j} \sum_{i \in \mathbb{J}} \alpha_{ui}. \tag{8}$$

If ϕ is a variable, which can be the vertical velocity (w), the liquid potential temperature (θ_l) or the total water mixing ratio (q), ϕ_i is ϕ in the i$^{\text{th}}$ cell of the LES field. $\phi_u(\Delta x)_i$ is the value of ϕ of the subgrid thermals of the i$^{\text{th}}$ cell of the LES grid, calculated for the Δx resolution. If $\alpha_u(\Delta x)_i = 1$, $\phi_u(\Delta x)_i$, otherwise, $\phi_u(\Delta x)_i$ is not defined. $\overline{\phi_u(\Delta x)}_j$ is the average value of $\phi_u(\Delta x)_i$ over the N_{uj} subgrid thermal cells of the j$^{\text{th}}$ cell of the grid of Δx resolution,

$$\overline{\phi_u(\Delta x)}_j = \frac{1}{N_{uj}} \sum_{i \in \mathbb{J}} \phi_u(\Delta x)_i. \tag{9}$$

2.2.3 Comparison of the CS$_{gz}$ Approach with the Literature

The subgrid non-local fluxes can be computed from these "subgrid thermal" fields, as

$$\overline{w'\phi'}^{\text{S,NL}}(\Delta x)_j = \overline{\alpha_u(\Delta x)}_j (\overline{w_u(\Delta x)}_j - \overline{w}_j)(\overline{\phi_u(\Delta x)}_j - \overline{\phi_e(\Delta x)}_j) \tag{10}$$

where $\overline{w'\phi'}^{\mathrm{S,NL}}(\Delta x)_j$ is the "subgrid thermal" vertical flux (superscripts, S, NL are subgrid and non-local) of ϕ, $\overline{w_u(\Delta x)}_j$ (respectively $\overline{\phi_u(\Delta x)}_j$) is the vertical velocity (respectively ϕ) averaged over the area of the cell covered by subgrid thermals and $\overline{\phi_e(\Delta x)}_j$ is ϕ averaged over the area of the cell not covered by subgrid thermals. Shin and Hong (2013) quantified the subgrid non-local fluxes in the grey zone by calculating terms in Eq. 10 where updraft values are provided by the $\mathrm{CS_{meso}}$ approach in subdomains of a given resolution. They proposed a curve fit of the subgrid non-local thermal flux of potential temperature as a function of the normalized resolution, viz.

$$\frac{<\overline{w'\theta'}^{\mathrm{S,NL}}(\Delta x)_j>}{<\overline{w'\theta'}^{\mathrm{NL}}(\Delta x)_j>} = 0.243 \left(\frac{\left(\frac{\Delta x}{h+h_c}\right)^2 + 0.936\left(\frac{\Delta x}{h+h_c}\right)^{\frac{7}{8}} - 1.110}{\left(\frac{\Delta x}{h+h_c}\right)^2 + 0.312\left(\frac{\Delta x}{h+h_c}\right)^{\frac{7}{8}} + 0.329} \right) + 0.757 \qquad (11)$$

where $\overline{w'\theta'}^{\mathrm{NL}}(\Delta x)_j$ is the total non-local flux computed from the $\mathrm{CS_{meso}}$ approach over the whole LES domain. The ratio between the subgrid non-local flux of potential temperature calculated by the $\mathrm{CS_{gz}}$ approach and the total non-local flux of potential temperature, calculated by the $\mathrm{CS_{meso}}$ approach applied to the whole domains of the five LES cases : IHOP at 1400 local time (LT), AMMA at 1200 LT, ARM at 1000 LT, Wangara at 1400 LT and BOMEX at 1000 LT, is consistent with the curve fit of Shin and Hong (2013), as shown in Fig. 2.

The method used by Shin and Hong (2013) does not provide any information on the structure of the residual subgrid thermals. Here the conditional sampling allows a diagnosis of the characteristics of the subgrid thermals at a given resolution in the grey zone and therefore also a computation of the exchange rates between the bulk subgrid thermal and the subgrid environment, which is not possible with the methodology of Shin and Hong (2013). The residual vertical velocity and the extension of the subgrid thermals, as well as exchanges of in-thermal air with the environment, are values for mass-flux parametrizations in the grey zone. For these reasons, in the following, the $\mathrm{CS_{gz}}$ approach is used.

3 Thermals in the Grey Zone of Convective Boundary-Layer Thermals

Here, the conditional sampling presented in Sect. 2.2.2 is applied to the five LES cases presented in Sect. 2.1.2 to quantify the subgrid thermal characteristics in the grey zone. The thermal field from the $\mathrm{CS_{meso}}$ approach is compared to the subgrid thermal field computed from the $\mathrm{CS_{gz}}$ approach.

3.1 Qualitative Description of the Subgrid Thermal Field

Figure 3 shows horizontal and vertical cross-sections of the thermal field ($\overline{\alpha}_j$) (in grey) and the subgrid thermal field ($\overline{\alpha_u(\Delta x)}_j$) (in black) for the ARM case at 1000 LT at several grid spacings in the grey zone of CBL thermals. At that time, the boundary-layer height reaches 950 m, with clouds overlaying the boundary layer; the top of the cloud layer is at about 2-km altitude. On the left of the vertical cross-sections [cf. Fig. 3(e–h)], two thermals extend to the boundary-layer top and cease penetration inside the cloud layer. Thermals that appear in the middle of the vertical cross-section belong to thermals that actually start at the ground but ahead of or behind the vertical cross-section.

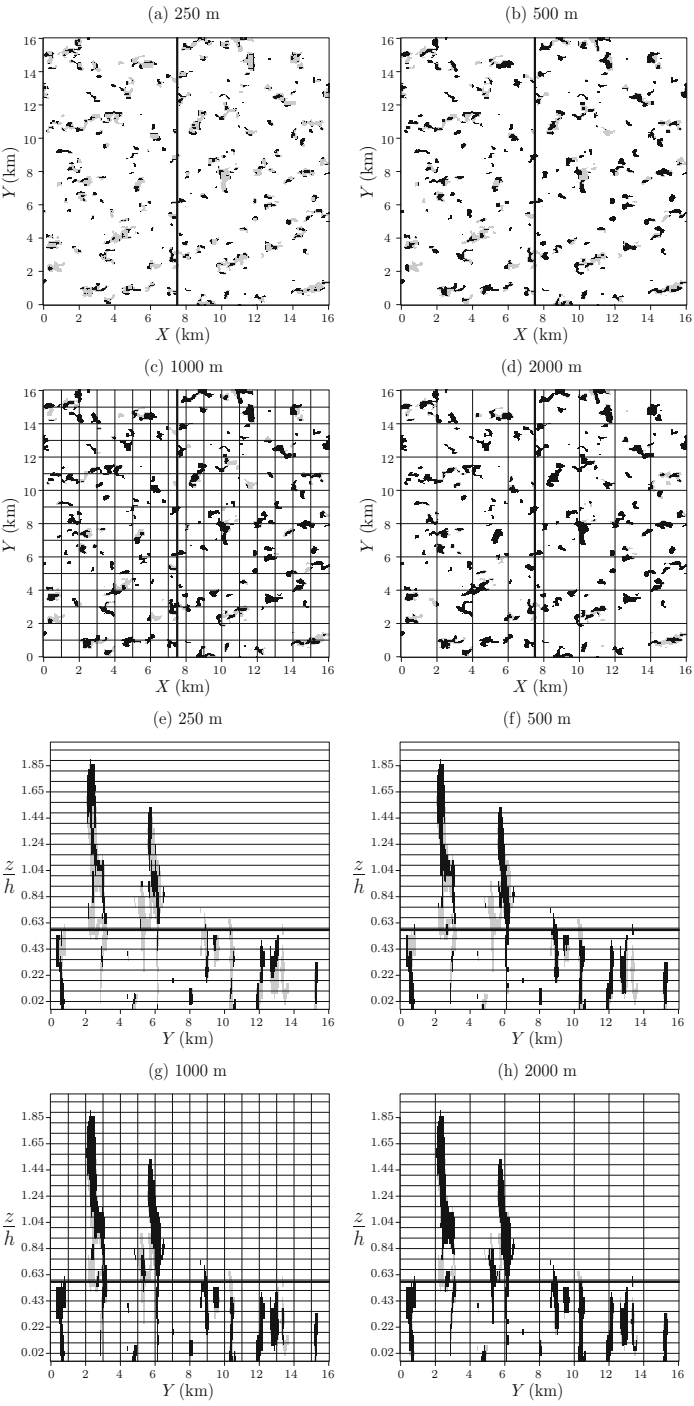

Fig. 3 **a–d** Horizontal cross-sections at 500-m altitude and **e–h** vertical cross-sections in the middle of the LES of the thermals (in *grey*) and subgrid thermals (in *black*) of the ARM case at 1000 LT. The Δx grid spacing is drawn for the two coarsest grid spacing plots. It is not added to the smallest grid spacing plots for legibility reasons. The *thick black line* indicates respectively the location of the vertical or horizontal cross-section

At each resolution, the subgrid thermal is in the core of the thermal. Indeed, the subgrid variability due to the non-local turbulence is found where the anomaly is at a maximum compared to the mean value, i.e. in the core. There is no subgrid thermal if there is no non-local turbulence detected at the mesoscale. As the mesh coarsens, the mesh contains both strong updrafts and downdrafts, the updrafts are more likely to be detected as subgrid thermals, because the mean value is negative or close to zero (cf. Fig. 3c, d). In both the horizontal and vertical cross-sections, one can see that at 250-m grid spacing, thermals are nearly always entirely resolved (cf. Fig. 3a, e), while at 2-km grid spacing, the thermals are almost entirely subgrid (viz. in black colour in Fig. 3d, h).

3.2 Thermal Fraction

For each j cell larger than the LES cells, one can compute the fraction of thermals by averaging the thermal field derived from the CS_{meso} approach ($\overline{\alpha}_j$, cf. Fig. 1) as well as the fraction of subgrid thermal by averaging the subgrid thermal field derived from the CS_{gz} approach ($\overline{\alpha_u(\Delta x)}_j$, cf. Fig. 1). Figure 4 shows histograms of thermals (in black) and the fraction of subgrid thermals (in white) for a grid spacing ranging from 62.5 m (LES) to 8 km (mesoscale). Only the ARM case at 1000 LT is shown here for illustration, but this represents the general behaviour of the simulations. As LES are assumed to have too fine a grid to contain subgrid thermals at the 62.5-m resolution, no subgrid thermal is defined and the histogram contains only ones (thermal meshes) or zeros (environmental meshes). However, in coarser grids, there is a difference between the fraction of thermals and the fraction of subgrid thermals, the first thermals including the second ones as illustrated previously. For the coarsest grid spacings, the thermal and subgrid thermal fractions are both 0.12 on average, which is consistent with Brown et al. (2002) and Pergaud et al. (2009) as the mesoscale thermals are entirely subgrid.

In the grey zone of CBL thermals, the thermal fraction ranges from zero to one as the thermals can partly or entirely fill the grid cell. The subgrid thermal fractions however range from 0 to 0.5 but always remain <0.5 whatever the grid spacing and the simulation. Indeed, if a thermal fills the whole grid cell, it is mostly resolved. The remaining subgrid part of it is the core of the thermal, where the velocity and the tracer concentration are larger than the average values over the cell. The area having these characteristics is by definition smaller than the grid cell; $\overline{\alpha_u(\Delta x)} = 0.5$ is the largest core of the thermal that is not resolved.

3.3 Subgrid Updraft Velocity Versus Resolved Vertical Velocity

The histograms of the vertical velocity of the subgrid thermals ($\overline{w_u(\Delta x)}_j$) are shown in Fig. 5, as well as the histograms of the resolved vertical velocity ($\overline{w}_j$) at a given grid spacing for all levels inside the boundary layer. This is illustrated for the ARM case at 1000 LT but is representative of all the LES. In the LES at 62.5-m resolution, there is no subgrid thermal by definition, and the vertical velocity inside the thermal is not defined. At this resolution, the histograms of the resolved vertical velocity (Fig. 5a) are typical of a CBL with both updrafts and downdrafts and a classical positively skewed histogram, which ranges from -4 m s^{-1} to 6 m s^{-1} (ARM case at 1000 LT).

For the grid spacings 125 m and 250 m, the thermals are mainly resolved; the vertical velocity of the subgrid thermals and the positive resolved vertical velocity have similar values. With coarser grid spacings, the thermals are less and less resolved; the resolved vertical velocity becomes increasingly smaller, while the velocity of the subgrid thermals remains large (up to 4 m s^{-1}) between 125-m to 1-km resolution. The resolved vertical velocity cannot

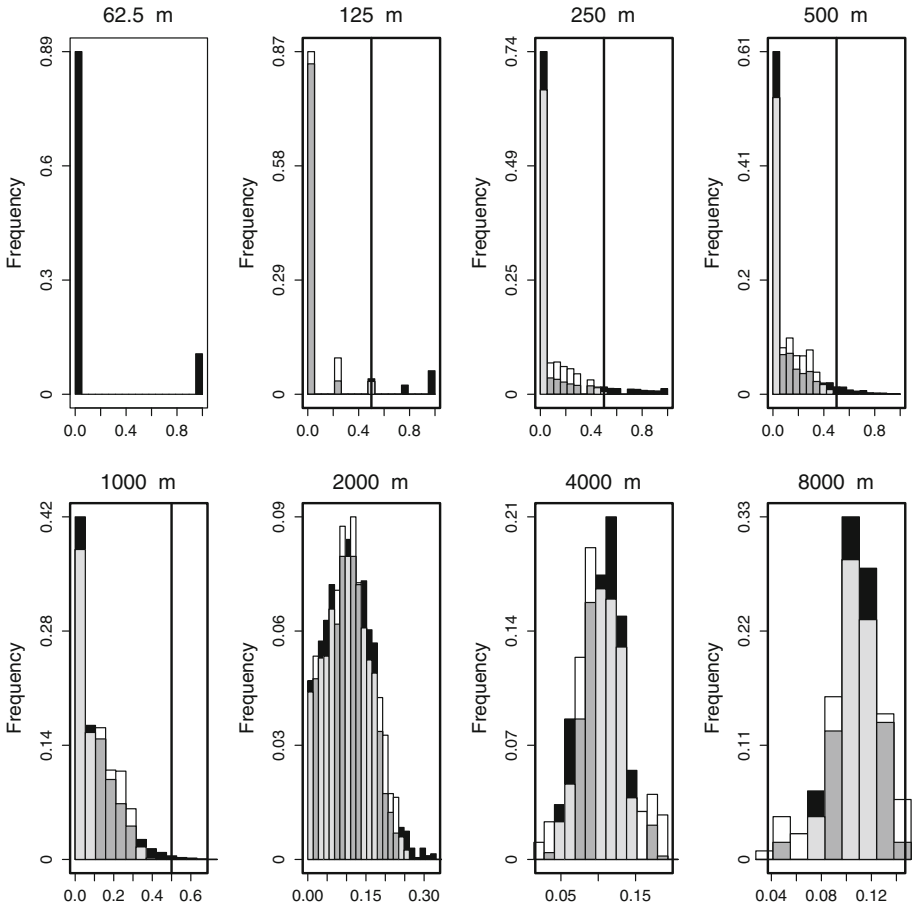

Fig. 4 Histograms of the fraction of the grid mesh covered by thermals ($\overline{\alpha}$, in *black*) and subgrid thermals ($\overline{\alpha_u(\Delta x)}$, in *white*) for grid cells ranging from 62.5 m to 8 km in the boundary layer (between 200-m and 1180-m altitude) of the ARM case at 1000 LT. The *grey areas* correspond to values where the bars of the two groups overlap: *light grey* when the subgrid thermal is under the thermal fraction and *dark grey* otherwise. The *vertical line* shows the 0.5 limit. Please note: the x and y axe ranges are different in each plot

be neglected compared to the velocity of the subgrid thermal. Finally, for the coarsest grid spacings ($\geq$ 2 km), the resolved vertical velocity is close to zero, as the cell contains both the thermal and the compensatory subsidence, and there is a large difference between the resolved vertical velocity and the velocity inside the updrafts. The resolved vertical velocity can be neglected compared to the velocity of the subgrid thermal.

3.4 Buoyancy of the Subgrid Thermal

The buoyancy of the subgrid thermals (B_u) is an important variable in mass-flux schemes. Indeed, it appears in the vertical velocity equation (Soares et al. 2004; Siebesma et al. 2007) and in the fractional entrainment/detrainment closure (Pergaud et al. 2009; Rio et al. 2010), viz.

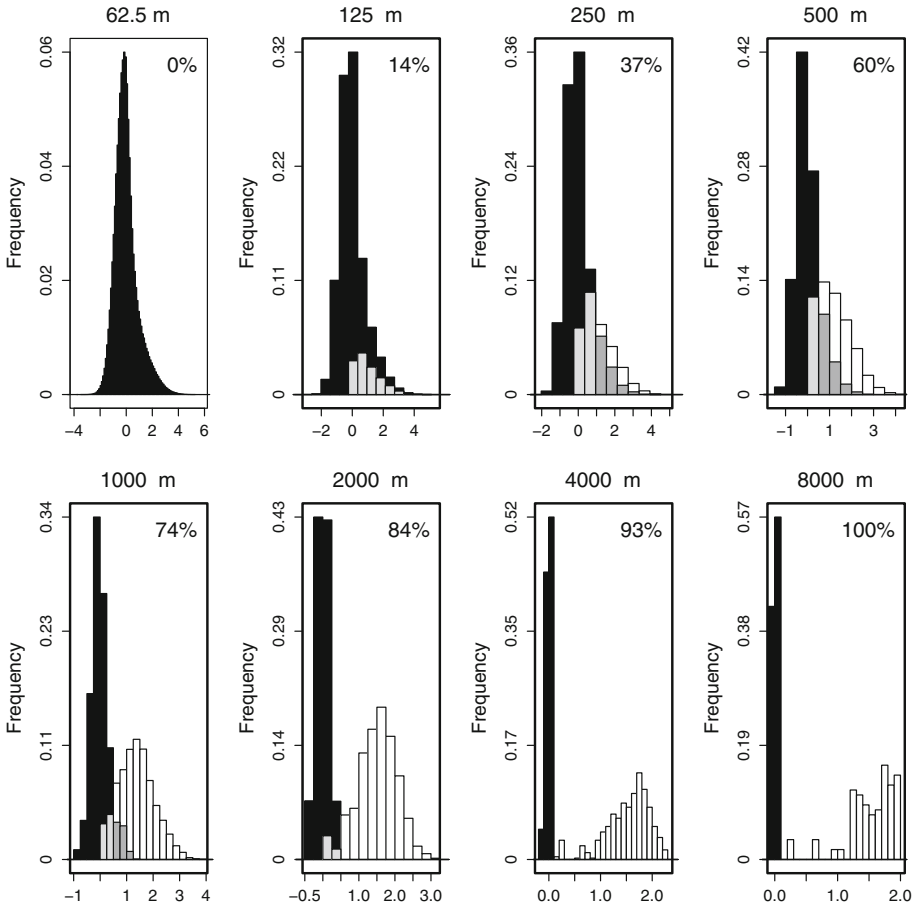

Fig. 5 Histograms of the vertical velocity of the subgrid thermals ($\overline{w_u(\Delta x)}$ (m s^{-1}), in white) and histograms of the resolved vertical velocity ($\overline{w}$ (m s^{-1}), in *black*) for grid meshes ranging from 62.5 m to 8 km in the boundary layer (between 200 and 1180-m altitude) of the ARM case at 1000 LT. The *grey areas* correspond to values where the *bars* of the two groups overlap, *light grey* when the subgrid thermal vertical velocity is under the total vertical velocity and *dark grey* otherwise. The fraction of the thermal which is subgrid is marked on the top right of the graphics. Please note: the x and y axe ranges are different in each plot

$$B_u(\Delta x)_j = \frac{g}{\theta_{v0}}(\overline{\theta_{vu}(\Delta x)_j} - \overline{\theta_v}_j) \tag{12}$$

where g is the acceleration due to gravity, θ_v is the virtual potential temperature and θ_{v0} is the reference state virtual potential temperature ($g/\theta_{v0} = 0.03$). Figure 6 shows vertical profiles of buoyancy of the subgrid thermals calculated as $<B_u> = (1/N_j)(\sum_j B_u(\Delta x)_j)$ for several horizontal resolutions.

The subgrid thermals are moister and warmer than the rest of the boundary-layer and therefore buoyancy is positive there whatever the horizontal resolution. For the coarsest grid spacings ($\geq$2 km), the cell contains numerous thermals. Thus the subgrid characteristics of the boundary layer do not vary from one resolution to another and thus neither do the buoyancy profiles.

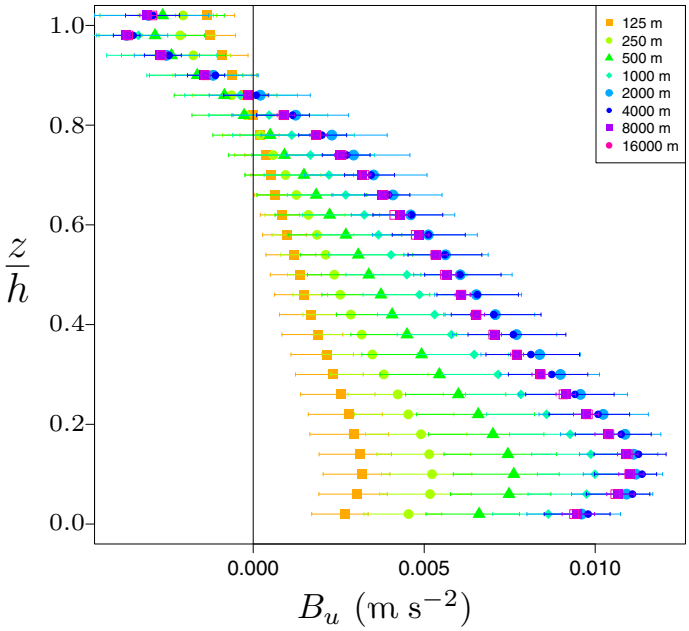

Fig. 6 Vertical profiles of buoyancy of the subgrid thermals ($B_u = 0.03(\overline{\theta_{vu}} - \overline{\theta_v})$) at several grid spacings from 125 m to 16 km of the ARM case at 1000 LT. The *horizontal bars* define the range between 25 and 75 % of the sample at each altitude. The points are the mean of the sample at each altitude

In the grey zone, the subgrid thermal buoyancy decreases with finer grid spacings. The difference in temperature and humidity between subgrid thermals and their environment is less and less important (not shown). Thus, the virtual potential temperature of the subgrid thermals does not depart much from the resolved virtual potential temperature, so the associated buoyancy is weaker than at mesoscales. The variance of the distribution of $B_u(\Delta x)_j$ is shown in Fig. 6 by the horizontal bars, and is larger in the grey zone than at mesoscales and small scales. The population of CBL thermals shrinks when the resolution increases from mesoscale to grey zone resolutions. Thus, the average grid-cell buoyancy, which strongly depends on the non-local turbulence, will differ from one cell to another in the grey zone. This strong variability is a characteristic of the grey zone that can be seen in all the parameters studied herein.

3.5 Mass Flux in the Grey Zone

The expression of the mass flux M_u for a given Δx grid spacing is (Siebesma and Cuijpers 1995),

$$M_u(\Delta x)_j = \overline{\alpha_u(\Delta x)_j}\,(\overline{w_u(\Delta x)_j} - \overline{w}_j), \tag{13}$$

and for simplicity's sake, the density ρ is not included, which does not change the conclusions of the study. As seen on the histograms of the vertical velocity in Fig. 5, the resolved vertical velocity cannot be considered negligible in the grey zone of CBL thermals, thus Eq. 13 is used as such. As for the buoyancy, at mesoscales (from 4- to 16-km grid spacings) the mass flux (not shown) does not depend heavily on the grid spacing and the variance is small. Indeed, the fraction of subgrid thermals and their velocity ($\overline{\alpha_u(\Delta x)_j}$ and $\overline{w_u(\Delta x)_j}$) remain

constant at mesoscales and the vertical velocity ($\overline{w_j}$) is negligible. However, from 125-m to 2-km resolution, the mass flux decreases in average over the whole boundary-layer depth and shows much variability as for the buoyancy in Fig. 6.

3.6 Entrainment/Detrainment

The buoyancy, mass flux and vertical velocity inside the thermals are regulated by exchanges of air between the thermals and their environment (entrainment E and detrainment D). In the mass-flux approach,

$$\frac{1}{M_u(\Delta x)_j}\frac{\partial M_u(\Delta x)_j}{\partial z} = \epsilon(\Delta x)_j - \delta(\Delta x)_j \tag{14}$$

where $\epsilon(\Delta x)_j$ is the entrainment rate ($\epsilon = E/M_u$) and $\delta(\Delta x)_j$ is the detrainment rate ($\delta = D/M_u$). As the $\mathrm{CS_{meso}}$ approach gives thermal boundaries, the $\mathrm{CS_{gz}}$ approach gives subgrid thermal boundaries, which allows quantification of the exchanges between the subgrid thermals and their environment. This allows direct computation of the $E(\Delta x)_j$ and $D(\Delta x)_j$. As shown by Romps (2011), the values obtained with this method (not shown) are larger than the values used in parametrizations, probably because they are calculated at the border of real inhomogeneous thermals while the parametrization demand transfers between two homogeneous areas. The rates are also two to three times larger than when using the traditional method of Siebesma and Cuijpers (1995),

$$\epsilon(\Delta x)_j = -\frac{1}{\overline{sv_u(\Delta x)}_j - \overline{sv_e(\Delta x)}_j}\frac{\partial \overline{sv_u(\Delta x)}_j}{\partial z}, \tag{15a}$$

and,

$$\delta(\Delta x)_j = \epsilon(\Delta x)_j - \frac{1}{M_u(\Delta x)_j}\frac{\partial M_u(\Delta x)_j}{\partial z}. \tag{15b}$$

This last method implies that the subgrid thermal field is quasi-stationary, which is not the case in the grey zone. Indeed, in the set of the five LES cases presented herein, the subgrid thermals move at a speed of several m s^{-1}, implying that they cross a 1-km grid cell in a time on the order of 1 min (the current timestep in the operational model AROME (Seity et al. 2010) is 50 s and its resolution is 1.3 km). Consequently, in the grey zone of CBL thermals, the thermal field is not quasi-stationary. Thus, the parametrization has to take the non-stationarity into account: either the timestep of the operational models must be reduced in order to be in conditions of quasi-stationarity or the non-stationarity must be parametrized. Consequently, the formulation of Siebesma and Cuijpers (1995) concerning entrainment/detrainment rates may not be valid.

However, despite those approximations, the two evaluations of the entrainment/detrainment rates (direct, Romps 2011 or by Siebesma and Cuijpers 1995) provide similar results in terms of the shape of $<\epsilon(\Delta x)_j>$ and $<\delta(\Delta x)_j>$ vertical profiles (not shown). Here we show in Fig. 7a, b the profiles from the method of Siebesma that are less scattered (thus more readable). Globally, the shape of the profiles of the entrainment and the detrainment rates remains the same with increasing resolution, but with increasing values consistent with the transfers being inversely proportional to the radius of the structures (Morton et al. 1956). However, at very fine resolution, the detrainment is stronger at the lowest levels. The detrainment rates increase slightly more than the entrainment rates at all altitudes and strongly increase at altitudes lower than 20 % of the boundary-layer height for resolutions

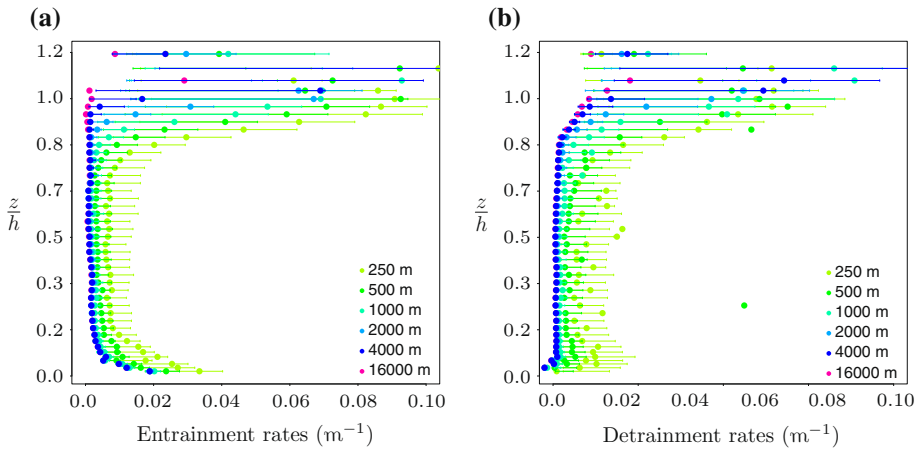

Fig. 7 Vertical profiles of **a** the entrainment rates and **b** the detrainment rates of grid spacing from 250 m to 16 km, in the IHOP case at 1200 LT for altitudes lower than 2 km. The *horizontal bars* define the range between 25 and 75 % of the sample at each altitude. The points are the mean of the sample at each altitude

finer than $0.5(h + h_c)$. This explains the reduction of the mass flux with the grid spacing in all studied cases.

Rio et al. (2010) assume that the entrainment rate is maximal when the thermal fraction is constant and there is no detrainment, implying

$$\epsilon_j = \frac{1}{\overline{M_u}_j} \frac{\partial \overline{M_u}_j}{\partial z} = \frac{1}{\overline{w_u}_j} \frac{\partial \overline{w_u}_j}{\partial z}. \tag{16}$$

They also assumed that the entrainment rate is proportional to and smaller than $\frac{1}{w_u}(\partial w_u)/(\partial z)$. In the grey zone, this approach leads to

$$\epsilon(\Delta x)_j = \frac{1}{\overline{w_u(\Delta x)}_j - \overline{w}_j} \frac{\partial \overline{w_u(\Delta x)}_j - \overline{w}_j}{\partial z}. \tag{17}$$

Figure 8 shows $< \epsilon(\Delta x)_j >$ as a function of $< 1/(\overline{w_u(\Delta x)}_j - \overline{w(\Delta x)}_j) \times \partial(\overline{w_u(\Delta x)}_j - \overline{w}_j)/\partial z >$ in the mixed layer ($0.15 \leq z/h \leq 0.80$). The finer the resolution, the less do the entrainment rates depend on $< 1/(\overline{w_u(\Delta x)}_j - \overline{w(\Delta x)}_j) \times \partial(\overline{w_u(\Delta x)}_j - \overline{w}_j)/\partial z >$. The lateral closure by entrainment and detrainment rates must be adapted because it depends on the resolution in the grey zone as shown here.

4 Discussion on Mass-Flux Schemes

In this section, the implications for the mass-flux scheme parametrizations of the previous results are discussed.

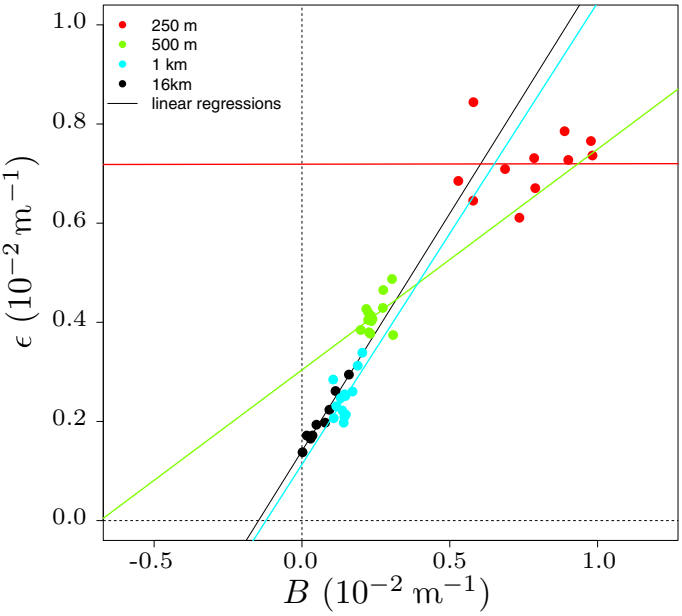

Fig. 8 The entrainment rates averaged at levels between $0.15h$ and $0.8h$ as a function of $B = <1/(\overline{w_u(\Delta x)}_j - \overline{w}_j) \times (\partial\overline{w_u(\Delta x)}_j - \overline{w}_j/\partial z)>$ at grid spacing from 250 m to 16 km, in the IHOP case at 1200 LT. Please note: the x and y axe ranges are different in each plot

4.1 Revision of the Assumptions of Most Mass-Flux Schemes

Honnert et al. (2011) proved that there is insufficient variability in the CBL when the model is operated at grey-zone resolution with the current version of the mass-flux scheme. This is due to the fact that a mass-flux scheme parametrizes several entirely subgrid structures at a resolution where it should simulate, at the most, one partly resolved thermal. The mass-flux scheme should adapt to the resolution and the subgrid thermal should disappear when the grid spacing becomes sufficiently fine (cf. Fig. 6).

At large scales, many mass-flux schemes are based on the equation for the evolution of a conservative variable ϕ (Siebesma and Holtslag 1996; Rio et al. 2010),

$$\frac{\partial\overline{\alpha}_j\overline{w_u}_j\overline{\phi_u}_j}{\partial z} = E\overline{\phi}_j - D\overline{\phi_u}_j, \tag{18}$$

which is based on several assumptions. Firstly, it is assumed that the area is divided into updrafts (the thermals) and environmental zones, both homogeneous, (the heterogeneities can be treated by the eddy-diffusivity part of the EDMF). Secondly, there is no non-local downdraft. Thirdly, the updraft field is assumed to be quasi-stationary, the resolved vertical velocity supposed to be zero and the thermal fraction is assumed to be small.

Arakawa et al. (2011) analyzed the grey zone of deep convection and showed that the cloud fraction could no longer be assumed small. Figure 1b shows that in the grey zone of CBL thermals the thermal fraction (in white in Fig. 1b) can be large. However, as part of the thermal is resolved, it is unclear whether the subgrid thermal fraction (in black in Fig. 1b) is negligible or not. Sect. 3.2 shows that the subgrid thermal fraction can reach 0.5, and a

consequence for the mass-flux scheme is that the value of ϕ over the environment of the updraft ($\overline{\phi_e(\Delta x)}_j$) cannot be substituted by $\overline{\phi}_j$ in Eq. 19.

Secondly, in mass-flux schemes at the mesoscale, the resolved vertical velocity can be neglected because the cell contains both the thermal and the compensatory subsidence, which results in a resolved vertical velocity close to zero or at least much smaller than the velocity of the updraft ($\overline{w_u(\Delta x)}_j$). However, Sect. 3.3 has shown that for grid sizes from 0.5 to $2(h+h_c)$, the resolved vertical velocity cannot be neglected compared to the velocity of the subgrid thermals.

Thus, the equation for the evolution of a conservative variable ϕ in the grey zone is,

$$\frac{\partial \overline{\alpha}_j (\overline{w_u}_j - \overline{w}_j)\overline{\phi_u}_j}{\partial z} = E\overline{\phi_e}_j - D\overline{\phi_u}_j. \tag{19}$$

4.2 Discussion on Closures

Equation 13 shows that, if the fraction of subgrid thermals remains relatively constant and if the differences between subgrid thermals and the resolved vertical velocity are reduced, then the mass flux ($M_u(\Delta x)_j$) becomes smaller. We have shown that, when the horizontal resolution increases, the fraction of subgrid thermals remains smaller than 0.5 (cf. Sect. 3.2) and the differences between subgrid thermals and the resolved vertical velocity is reduced (cf. Sect. 3.3). Consequently, the mass flux decreases with increasing resolution. However, in parametrizations the mass flux is not calculated from the thermal fraction and the vertical velocity but from the entrainment/detrainment rates.

The diagnostics of entrainment and detrainment rates calculated in Sect. 3.6 are not made to be directly used in a parametrization. As a closure and as a subgrid parameter, they are dedicated to being tuned to produce the best large-scale parameter possible. However, the behaviour of the profiles with increasing resolution can give direction as to how to adapt parametrizations to the grey zone. In Sect. 3.6, it is shown that the shape of the entrainment and detrainment rates remains the same with increasing resolution, but that the rates increase and the detrainment must increase more rapidly. Moreover, at a given altitude the scatter of the lateral exchanges in the grey zone (cf. Fig. 7a, b) is smaller than that of the mass flux (see Fig. 9b described hereafter). So the variability of the mass flux may not result from only the variability of the entrainment and detrainment rates. This shows that the parametrization of the lateral closure can then remain the same as at the mesoscale by increasing the constants with horizontal resolution. The surface closure has to evolve too.

The triggering controls the activation of the mass-flux scheme at the surface while the closure controls its intensity. Often the boundary-layer mass-flux scheme triggers as soon as the surface sensible heat flux is positive while the intensity of the mass flux at the ground is proportional to the convective velocity scale (see Pergaud et al. 2009 for example).

Firstly, concerning the closure, Fig. 9a shows the subgrid mass flux normalized by the convective velocity scale as a function of the normalized resolution in the IHOP case at 1200 LT, and in the ARM case at 1400 LT in the mid boundary layer. The mass flux normalized by the convective velocity scale in both the IHOP and ARM cases is dependent on the resolution normalized by the height of the thermals: it is constant at the mesoscale and larger than in LES. Here the mass flux is computed in the middle of the CBL. It cannot be diagnosed directly at the ground, where there is no formed thermal, where the turbulence is more strongly dependent on the subgrid turbulence scheme. The normalized mass flux as a function of the normalized resolution has the same shape at all altitudes in the boundary layer (not shown). Therefore, here we propose to make the constant of proportionality between the mass flux at

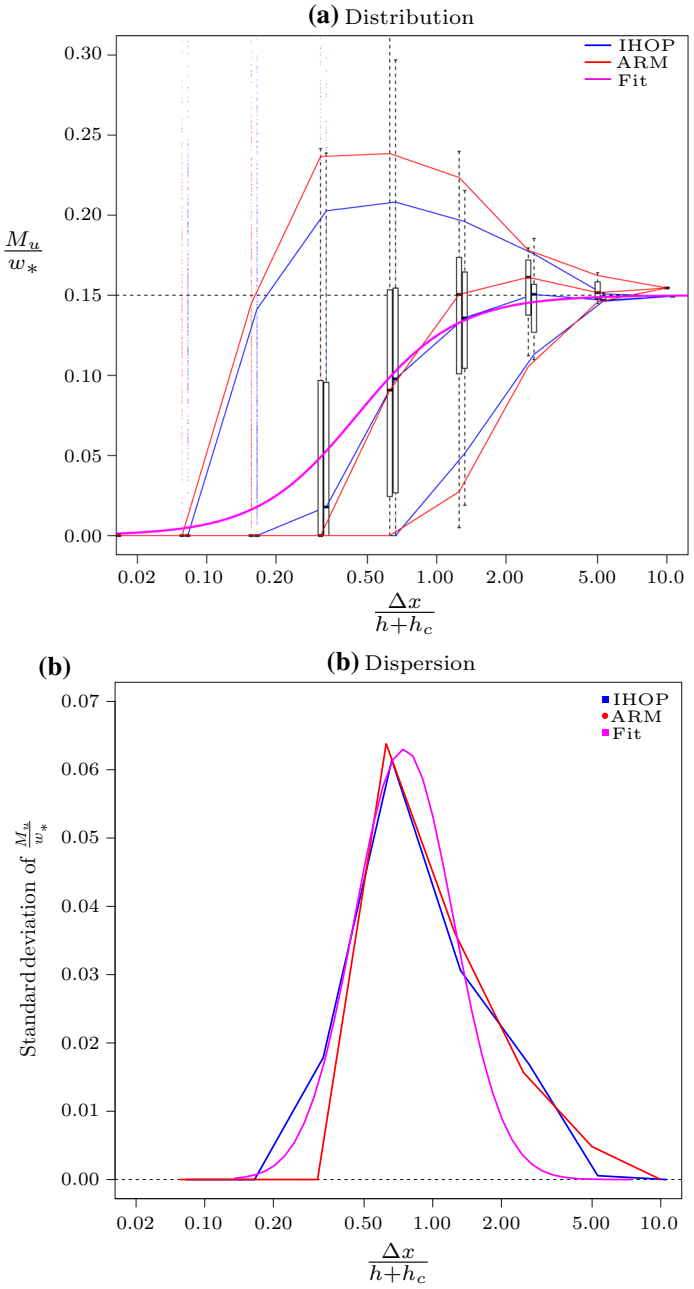

Fig. 9 **a** Mass flux of the subgrid thermals normalized by the convective velocity scale for grid cells ranging from 250 m to 8 km in the mid boundary layer of the ARM case at 1400 LT (*blue* points) and the IHOP case at 1200 LT (*red* points) as a function of $\Delta x/(h + h_c)$. *Boxplots* of the data (one per case): the box shows 50 % of the data and the line 99.3 %. Median, quantile 5 % and 95 % in (*red* and *blue*) lines. A fit of the data (see text for more details) is in *magenta*. **b** Standard deviation of the same data in the same colours as in **a** as a function of the normalized horizontal resolution

the ground and the convective velocity scale (computed at ground level for the whole domain, w_*) dependent on the resolution by this function,

$$\frac{M_u}{w_*} = C\left(1 + \tanh(\ln(\frac{\Delta x}{h + h_c}) + 0.8)\right), \tag{20}$$

and in the magenta fit plotted in Fig. 9a, $C = 0.075$. We propose to use this function in the parametrization so as to be scale-aware.

Moreover, the subgrid mass-flux variability is larger in the grey zone than in the LES and at the mesoscale. This is visible in Fig. 9b that shows the standard deviation of the mass flux normalized by the convective velocity scale $\sigma(\frac{M_u}{w_*})$ as a function of the normalized resolution in the IHOP case at 1200 LT and the ARM case at 1400 LT in the mid CBL. The large variability in the grey zone is also visible in the buoyancy (cf. Fig. 6) and the entrainment (cf. Fig. 7), and it is consistent with Dorrestijn et al. (2013) who showed that the heat-flux variability is larger in the grey zone. The fit of the data of Fig. 9b is,

$$\sigma\left(\frac{M_u}{w_*}\right) = 0.063 \exp\left(\frac{-(\ln(\frac{\Delta x}{h+h_c}) + 0.29)^2}{0.5}\right). \tag{21}$$

In these conditions, stochastic parametrizations could be useful, as they allow different closures with the same forcing.

Secondly, concerning the triggering, at the mesoscale each model column contains thermals when the surface flux is positive; this is not the case in the grey zone where, even with a positive surface flux, there are columns that contain no thermal at all. Figure 10 shows histograms of resolved variables at the ground ($\overline{\theta}_j$, $\overline{q}_j$ and $\overline{w}_j$ and the TKE, e_j). The cells having subgrid thermals in the column above them are in white, while those in a column that contains no thermal at all are in black. This confirms that, unlike at the mesoscale, at 500-m resolution, there are cells where there is no thermal at all, $\overline{\alpha_u(\Delta x)}_j = 0$ in black in Fig. 10). The proportion of model columns containing no thermal depends on the resolution; it is 5 % of the cells at 500-m resolution, 20 % at 250-m resolution (not shown) and 30 % at 125-m resolution. Thus, in the grey zone, the triggering of the scheme at the ground depends on the horizontal resolution.

In addition, the existence of subgrid thermals in a column does not seem to depend on the value of the resolved parameters either at the ground (in Fig. 10) or at higher levels (not shown). In these conditions, the triggering of the scheme depends on factors other than the characteristics of the resolved field, which confirms the need for stochastic triggering of the mass flux. Moreover, Rochetin et al. (2014) prove that stochastic schemes are scale adaptive, as the probability of triggering in the domain remains the same when the resolution changes. Such stochastic parametrizations have already been proposed for deep convection parametrization (Craig and Cohen 2006; Rochetin et al. 2014; Sakradzija et al. 2015).

5 Conclusions and Perspectives

The grey zone of CBL thermals is a range of scales for which the coarsest boundary-layer eddies (thermals) are partly resolved. Thermal plumes have been studied herein in the grey zone of CBL thermals, and to determine the characteristic of the subgrid component of the thermals, the conditional sampling of Couvreux et al. (2010) is adapted to detect subgrid thermals for a given resolution. Characteristics of these structures are listed, as well as their

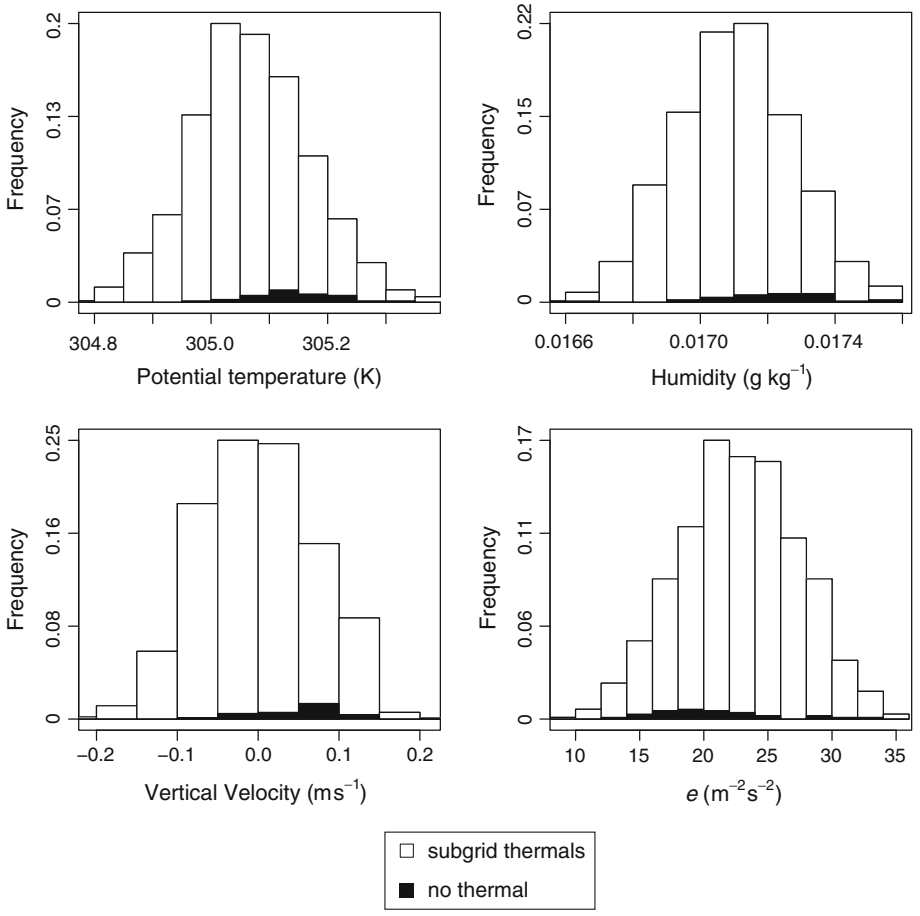

Fig. 10 Histograms of potential temperature (K), water vapour mixing ratio (g kg^{-1}), vertical velocity (m s^{-1}) and resolved TKE, e (m^2 s^{-2}) at the ground at 500-m resolution in the ARM case at 1000 LT. In *black*, the cells for which there is no thermal above them. In *white*, cells with a subgrid thermal above them

sensitivity to the horizontal resolution; it appears that traditional assumptions used to simplify the mass-flux equations are not valid in the grey zone.

In the grey zone, the thermal fraction is not negligible; however, as the thermals are partly resolved, the subgrid thermal fraction remains <0.5. Moreover, the representation of dynamics in the model resolves a part of the thermals and the resolved vertical velocity is no longer close to zero. Consequently, the resolved vertical velocity is no longer small compared to the updraft velocity. The entrainment and detrainment rates should be larger with finer resolution. The detrainment should become larger more rapidly than the entrainment, leading to a decrease in the mass flux.

In the grey zone of CBL thermals, subgrid thermals are not present in each grid cell, therefore a stochastic approach seems pertinent to determine the triggering of the scheme. In addition, a closure of the scheme is proposed that allows a reproduction of the dependency of the intensity of the mass flux as a function of the normalized resolution. These modifications

are currently being tested within the EDMF of Pergaud et al. (2009) in the Meso-NH and AROME models.

Appendix 1 Notations used in this article

$\mathbb{D}$	Domain size
$\mathbb{J}$	LES domain of one Δx-grid cell
Δx	Horizontal grid spacing
z	Altitude
h	Boundary-layer height
L_O	Obukhov lenght
h_c	Depth of the cloud layer
sv	Tracer concentration
w	Vertical velocity
q	Total water mixing ratio
θ_v	Virtual potential temperature
θ_l	Liquid potential temperature
g	Standard gravitational acceleration
ρ	Volumic mass of the air
α	Fraction of a grid cell covered by convective thermal, LES field not depending on Δx
i	LES-grid cell number
j	Δx-Grid cell number
ϕ	A thermodynamical variable
ϕ_i	ϕ of the ith cell of a LES grid
ϕ_j	ϕ of the jth cell of Δx grid spacing
α_{ui}	Grid cell covered by convective subgrid thermal, LES field depending on Δx
ϕ_{ui}	$\alpha_u \times \phi$ of the ith cell of the LES
$< \phi >$	Average value of ϕ over the whole horizontal domain
$\overline{\phi}$	Average value of ϕ (reference resolved value of ϕ) over a cell of Δx Grid spacing
N	Number of LES cell at one level
N_j	Number of LES cell in a $\mathbb{J}$ domain
N_{uj}	Number of LES cell occupied by a subgrid thermal in a cell of Δx Horizontal resolution
M_u	Mass Flux
B_u	Buoyancy inside the updraft
E	Entrainment term
D	Detrainment term
ϵ	Entrainment rate
δ	Detrainment rate
H_{0v}	Averaged surface buoyancy flux
E_0	Averaged surface humidity flux
w_*	Averaged convective velocity scale computed at ground level
u_*	Averaged friction velocity computed at ground level

References

Arakawa A, Jung J-H, Wu C-M (2011) Toward unification of the multiscale modeling of the atmosphere. Atmos Chem Phys 11:3731–3742

Arakawa A, Wu C-M (2013) A unified representation of deep moist convection in numerical modeling of the atmosphere. Part I. J Atmos Sci 70:1977–1992

Brown AR, Cederwall RT, Chlond A, Duynkerke PG, Golaz J-C, Khairoutdinov M, Lewellen DC, Lock AP, Macvean MK, Moeng C-H, Neggers RAJ, Siebesma AP, Stevens B (2002) Large-eddy simulation of the diurnal cycle of shallow cumulus convection over land. Q J R Meteorol Soc 128:1075–1093

Canut G, Couvreux F, Lothon M, Pino D, Said F (2012) Observations and large-eddy simulations of entrainment in the sheared sahelian boundary layer. Boundary-Layer Meteorol 142:79–101

Cheng A, Xu K-M, Stevens B (2009) Effects of Resolution on the simulation of boundary-layer clouds and the partition of kinetic energy to subgrid scales. J Adv Model Earth Syst 2:21. doi:10.3894/JAMES.2010.2.3

Clarke RH, Dyer AJ, Reid DG, Troup AJ (1971) The Wangara experiment: Boundary layer data. Division Meteorological Physics Paper, CSIRO 19: Australia

Couvreux F, Guichard F, Redelsperger J-L, Kiemle C, Masson V, Lafore J-P, Flamant C (2005) Water vapour variability within a convective boundary-layer assessed by large-eddy simulations and IHOP 2002 observations. Q J R Meteorol Soc 131:2665–2693

Couvreux F, Hourdin F, Rio C (2010) Resolved versus parametrized boundary-layer plumes. Part I: A parametrization-oriented conditional sampling in large-eddy simulations. Boundary-Layer Meteorol 134:441–458

Craig GC, Cohen BG (2006) Fluctuations in an equilibrium convective ensemble. Part I: Theoretical formulation. J Atmos Sci 63:1996–2004

Cuxart J, Bougeault P, Redelsperger J-L (2000) A turbulence scheme allowing for mesoscale and large-eddy simulations. Q J R Meteorol Soc 126:1–30

De Roode SR, Duynkerke PG, Jonker HJJ (2004) Large-eddy simulation: how large is large enough? J Atmos Sci 61:403–421

Deardorff JW (1972) Numerical investigation of neutral and unstable planetary boundary layers. J Atmos Sci 29:91–115

Dorrestijn J, Crommelin DT, Siebesma AP, Jonker HJJ (2013) Stochastic convection parametrization estimated from high-resolution model data. Theor Comput Fluid Dyn 27:133–148

Frech M, Mahrt L (1995) A two-scale mixing formulation for the atmospheric boundary layer. Boundary-Layer Meteorol 73:91–104

Honnert R, Masson V, Couvreux F (2011) A diagnostic for evaluating the representation of turbulence in atmospheric models at the kilometric scale. J Atmos Sci 68:3112–3131

Hourdin F, Couvreux F, Menut L (2002) Parameterization of the dry convective boundary layer based on a mass flux representation of thermals. J Atmos Sci 59:1105–1122

Lafore JP, Stein J, Asencio N, Bougeault P, Ducrocq V, Duron J, Fischer C, Héreil P, Mascart P, Masson V, Pinty JP, Redelsperger JL, Richard E, Vila-Guerau de Arellano J (1998) The Méso-NH atmospheric simulation system. Part I: Adiabatic formulation and control simulation. Ann Geophys 16:90–109

Morton B, Taylor G, Turner J (1956) Turbulent gravitational convection from maintained and instantaneous sources. Proc R Soc Lond, pp 1–23

Pergaud J, Masson V, Malardel S, Couvreux F (2009) A parametrization of dry thermals and shallow cumuli for mesoscale numerical weather prediction. Boundary-Layer Meteorol 132:83–106

Peter P. Sullivan, Edward G. Patton (2008) A highly parallel algorithm for turbulence simulations in planetary boundary layers: results with meshs up to 1024^3. National Center for Atmospheric Research, Boulder, CO. In: 16th Symposium on Boundary Layer and Turbulence, AMS

Redelsperger JL, Thorncroft CD, Lebel T, Diedhiou A, Parker DJ, Polcher J (2006) African monsoon multidisciplinary analysis an international research project and field campaign. Bull Am Meteorol Soc 87(12):1735–1746

Rio C, Hourdin F, Couvreux F, Jam A (2010) Resolved versus parametrized boundary-layer plumes. Part II: Continuous formulations of mixing rates for mass-flux schemes. Boundary-Layer Meteorol 135:469–483

Rochetin N, Couvreux F, Grandpeix J-Y, Rio C (2014) Deep convection triggering by boundary layer thermals. Part I: LES analysis and stochastic triggering formulation. J Atmos Sci 71:496–514

Romps D (2011) A direct measure of entrainment. J Atmos Sci 68:2009–2025

Sakradzija M, Seifert A, Heus T (2015) Fluctuations in a quasi-stationary shallow cumulus cloud ensemble. Nonlinear Process Geophys 22:65–85

Seity Y, Brousseau P, Malardel S, Hello G, Benard P, Bouttier F, Lac C, Masson V (2010) The AROME-France convective scale operational model. Mon Weather Rev 139:976–991

Shin H, Hong S (2013) Analysis on resolved and parametrized vertical transports in the convective boundary layers at the gray-zone resolution. J Atmos Sci 70:3248–3261

Siebesma AP, Bretherton CS, Chlond A, Cuxart J, Duynkerke PG, Jiang H, Khairoutdinov M, Lewellen D, Moeng C-H, Sanchez E, Stevens B, Stevens DE (2003) A large eddy simulation intercomparaison study of shallow cumulus convection. J Atmos Sci 60:1201–1219

Siebesma P, Soares PMM, Teixeira J (2007) A combined eddy-diffusivity mass-flux approach for the convective boundary layer. J Atmos Sci 64:1230–1248

Siebesma P, Cuijpers JWM (1995) Evaluation of parametric assumptions for shallow cumulus convection. J Atmos Sci 53:650–666

Siebesma AP, Holtslag AAM (1996) Model impacts of entrainment and detrainment rates in shallow cumulus convection. J Atmos Sci 53:2354–2364

Soares PMM, Miranda PMA, Siebesma AP, Teixeira J (2004) An eddy-diffusivity/mass-flux parametrization for dry and shallow cumulus convection. Q J R Meteorol Soc 130:3365–3383

Stull RB (1984) Transilient turbulence theory. Part I: The concept of eddy-mixing across finite distances. J Atmos Sci 41:3351–3366

Weckwerth TM, Parsons DB, Koch SE, Moore JA, Lemone MA, Demoz BR, Flamant C, Geerts B, Wang J, Feltz W (2004) An overview of the international H2O project (IHOP 2002) and some preliminary highlights. Bull Am Meteorol Soc 85:253–277

Wyngaard JC (2004) Toward numerical modelling in the 'Terra Incognita'. J Atmos Sci 61:1816–1826